Received: 20 February 2023 | Revised: 23 July 2023 | Accepted: 30 August 2023

The Journal of Engineering

DOI: 10.1049/tje2.12310

The Institution of Engineering and Technology WILEY

ORIGINAL RESEARCH

A novel fault location strategy based on Bi-LSTM for MMC-HVDC systems

Jude Inwumoh | **Craig Baguley** | **Udaya Madawala** | **Kosala Gunawardane**

Department of Electrical Electronics, Auckland University of Technology, Auckland, New Zealand

Correspondence
Jude Inwumoh, Department of Electrical Electronics, Auckland University of Technology, Auckland, New Zealand.
Email: jinwumoh@aut.ac.nz

Abstract
The integration of modular multilevel converters (MMCs) with high voltage direct current (HVDC) transmission systems is an efficient method for transporting electricity from distant renewable energy sources to demand centres. However, MMC-HVDC systems face reliability challenges during DC overcurrent faults, often caused by component failures that can lead to HVDC network shutdowns. Consequently, a reliable fault location approach is crucial for grid protection and restoration, aiding in fault isolation and alternate power flow identification. Conventional fault location methods struggle with manual protective threshold setting, susceptibility to fault resistance and noise, and the need for communication channels, resulting in signal delays. In multi-terminal HVDC networks, fault location becomes even more complex due to poor selectivity and sensitivity in traditional schemes. This study proposes a robust fault location approach based on bidirectional long short-term memory (bi-LSTM). The method offers a simplified decision-making model with low computational requirements, utilizing fault features from one end of the network, eliminating the need for a communication channel. Remarkably, this approach achieves high fault location accuracy, even with varying fault types, resistances, and noise levels, as demonstrated by an MSE of 0.006 and a percentage error below 1% in simulations conducted using a real-time simulator with MATLAB/Simulink.

1 | INTRODUCTION

High voltage direct current (HVDC) systems are one of the most promising technologies in the power industry. This technology can be used in overhead transmission lines and submarine cables for long-distance renewable energy transmission since it can offer flexible and bulk power transfer at reduced losses [1]. However, as most conventional power systems are AC, integrating an HVDC transmission system requires AC/DC conversion [2]. This conversion is made possible with the aid of a line commutated converter (LCC). LCC is a well-established converter technology used for HVDC deployment. However, LCC based HVDC systems are faced with challenges such as the need for bulky filters, commutation failure, and frequent DC polarity changes for power reversal [3].

As a result, the modular multilevel converter (MMC) was chosen as a better alternative to LCC, with the ability to produce bidirectional control capability and reduced harmonic distortion with no filter requirement [4]. However, MMC based HVDC transmission networks have struggled to sustain direct current (DC) short circuit faults, which pose a severe threat to the safety and stability of the network [5]. DC faults are inevitable and can result from misfires and flashovers of the MMC rectifier stations or malfunctioning of the valves and controllers in the MMC converter. In addition, the DC fault could be caused by natural causes, such as earthquakes, and human errors, such as war and sabotage. If these faults are not isolated, they can damage the components of the MMC, shutting down the entire network, and hampering power supply reliability. As a result of the negative impact of this fault, it is vital to classify and locate the exact point of fault impact on the network to aid fault isolation while an alternative path is provided for power flow. Thus, a safe and reliable operation is guaranteed, as the components in the MMC-HVDC network are protected from further harm. Moreover, estimating the fault location reduces maintenance costs and the time spent on repairs. Considering that MMC-HVDC transmission lines are very long, accurately locating a fault is challenging. For example, in 2015, the 295 km long Basslink HVDC transmission between Tasmania and Australia's mainland was affected by a fault. It took approximately 500 h for the contractors (Alcatel-Lucent) to locate the fault using extra hardware at the repeater stations [6]. This method increases the cost of the fault location. In addition, an extra-long cable, such as the 2500 km long Porto Velho-Sao Paulo, would be more complex and expensive. Such a lengthy disruption of the power supply is usually unacceptable. Hence, it is crucial to investigate a prompt and cost-effective approach for accurately locating DC faults.

Several fault location methods for HVDC transmission lines have been proposed. The travelling wave (TW) method is the most common among conventional techniques. This method's accuracy depends on the arrival time and velocity of the reflected fault wave [7]. The TW method struggles to differentiate the waves from a system terminal from those of a fault [8]. To improve the accuracy of the TW method, a double-ended TW method was proposed, in which fault waves from the rectifying and inverting terminals of the MMC-HVDC network are synchronised using a Global Positioning System (GPS) and a communication channel [9]. However, the cost of installing GPS and communication channels are the two major drawbacks of this method. Besides, a weak wave is generated for a high resistance fault, which can easily be attenuated, leading to a significant location error. Apart from the TW method, the impedance method has been used to locate faults in MMC-HVDC systems. In [10], an impedance-based method was used to locate high-resistance and remote faults. This technique measures the characteristic harmonics of the fault current and voltage in the HVDC transmission line to obtain the fault distance. The method is easy to apply. However, they are susceptible to noise signals and the operating state of the MMC converter. In [11], the Pearson correlation coefficient of voltage signals was another fault location method for MMC-HVDC systems. Its location process is quite challenging to implement because the voltage signals are easily disturbed by the actions of fault protection devices. In addition, the Pearson correlation coefficient changes with voltage ripples, even when the rate of change of the voltage is the same. This could lead to a miscalculation of the fault location. In [12], a fault location based on electromagnetic time reversal (EMTR) was proposed. This method uses an approach similar to TW fault location techniques by refocusing the peak energy amplitude from time-reversed waves to locate the unknown fault distance. However, it fails to accurately locate high impedance faults, and requires numerous backpropagation simulations to identify the fault location. In [13], the Prony algorithm was used to locate faults using the principal components of natural frequencies. However, it is prone to location errors since the Prony model is numerically ill-conditioned, non-strict, and sensitive to noise.

With the rapid development of artificial intelligence (AI), AI algorithms have been applied to various fault location tasks, such as fault location in power systems. However, most of these algorithms cannot capture time-series features of voltage or current signals. For example, an improved extreme learning machine [14] was designed to locate faults; however, it did not consider time-series features. In [15], the Decision Tree Regression (DTR) method was used to extract the characteristics of the voltage and current signals to determine the fault location. However, for some experimental samples, the method produced significant errors. In [16], support vector machine (SVM) was used to identify the fault segment, while TW analysis was used to obtain the location of the fault. The analysis was limited to only a two-terminal network, and the study did not investigate the high resistive fault. Considering the above limitation, [17] proposes the use of a genetic algorithm to locate HVDC faults using the voltage profile in the frequency domain. However, the sampling rate of the algorithm was too high, which affected the accuracy of the method. In [18], a back propagation neural network was used to achieve fault location on an MMC HVDC system, but it was at the expense of high computational burdens and reduced accuracy. In [19], fault signals were processed through empirical mode decomposition (EMD) and used to train a deep learning-based convolutional neural network (CNN). CNN classification and linear regression mechanisms were used to determine the fault location on the HVDC network. The model also considers the impact of high impedance ground faults, but it cannot automatically adapt to different fault lines. Moreover, this technique uses complex feature extraction and a working algorithm. There is a need to eliminate the feature extraction part and work directly on operational data since it increases the complexity and computational burden of the scheme. Therefore, a research gap exists in locating faults in HVDC grid networks using deep learning-based AI algorithms.

This study proposes a new deep learning AI-based fault location method inspired by bi-LSTM. bi-LSTM has an advantage over other deep learning algorithms since it has direct access to all the gate activation functions, thus ensuring frequent updating of its memory cells so that the algorithm recognises patterns over a long period, aiding desired system performance. In addition, the algorithm uses simple addition and multiplication to update the cell states, thereby requiring only minor adjustments and a lower computational burden.

Bi-LSTM can classify fault lines and locate fault distances using a simplified extraction and analysis approach on fault data from only the rectifying end of the MMC-HVDC network, thus eliminating the need for a communication channel. Furthermore, the proposed algorithm learns the time series of the fault current samples from a real-time simulator of bipolar and four-terminal MMC-HVDC systems based on Artemis and SSN benchmarks. The accuracy of the proposed technique was verified for different fault types, fault impedances, and noise levels. From the above statements, the main contributions of this work are summarised as follows: A simple and robust fault classification and location scheme are proposed to handle high-resolution time step data with the exclusion of complex feature extraction, thus eliminating the issue of

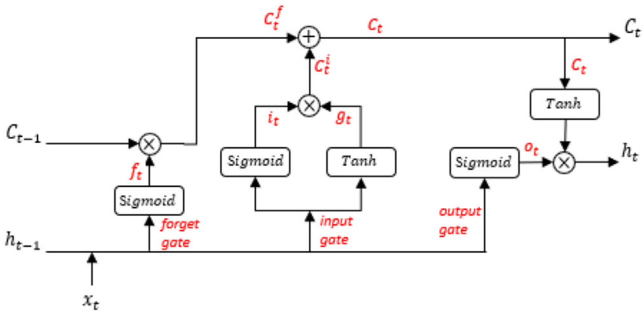

FIGURE 1 The structure of LSTM.

computational burden. In addition, the scheme is resilient against varying fault impedances, noise, transmission line parameters, and operating conditions. This approach can eliminate the issue of vanishing gradients affecting the deployment of Recurrent Neural Networks (RNN) in practical systems. Finally, the proposed algorithm can adapt to a more complex multiterminal MMC-HVDC network with a location percentage error of less than 1%.

The rest of the paper is structured as follows: Section 2 presents a theoretical analysis of the proposed scheme, and Section 3 provides a detailed analysis of the fault location methodology. Section 4 discusses the system under test and the data acquisition process. Section 5 presents the simulations and results, as well as a set of comparisons with other fault location methods. Finally, the conclusions are presented in Section 6.

2 | DESCRIPTION OF THE PROPOSED SCHEME

The long short term memory (LSTM) algorithm is a deep learning algorithm integrated into MMC-HVDC to locate DC faults in the network. The algorithm is a new type of recurrent neural network (RNN). An RNN is an improved version of a convolutional neural network (CNN), which is one of the most popular deep learning algorithms. The RNN uses previous output data to forecast new data. This ability has led to significant improvements in time-series forecasting tasks. However, the RNN still suffers from gradient disappearance [20]. A condition where the weights of the neurons are unable to learn and update as the time step increases. This condition is severe because the learning rate of the network decreases, and the network may fail during the training phase. RNNs also require high computing power during the training of data for large scale implementations. These drawbacks of RNN can be linked to the fact that the recurrence of data is achieved using a single layer. LSTM solves the issue of RNN gradient disappearance using three different gates with separate activation functions to continuously update the data. Moreover, LSTM has a memory block that can hold information for a long time step; thus, it is called Long Memory.

The gates in the LSTM are the forget, input, and output gates, as shown in Figure 1. These gates control the flow of information in the LSTM. The "forget" gate can be used to remove unwanted data. It uses a sigmoid activation function to refresh the memory of the LSTM. The input gate is located immediately after the forget gate. This gate controls whether the memory should be updated, and the elements required for the update. The output gate determines the features that are sent to the hidden state.

From Figure 1, x_t is the current time step of the input data, whereas the previous time step of the cell state and the hidden layer are C_{t-1} and h_{t-1}, respectively. The current hidden state, h_t, of the LSTM can be computed by updating the weight and bias parameters of each gate as shown below:

Forget gate,

$$f_{sigmoid} = \left(\omega_{fh} + \omega_{fx} + b_f\right) \tag{1}$$

By passing the inputs (h_{t-1} and x_t) through the function, (2) can be obtained:

$$f_t = \sigma\left[\left(\omega_{fh} + h_{t-1}\right) + \left(\omega_{fx} + x_t\right) + b_f\right] \tag{2}$$

$$C_t^f = C_{t-1} \times f_t \tag{3}$$

Input gate,

$$i_{sigmoid} = (\omega_{ih} + \omega_{ix} + b_i) \tag{4}$$

$$i_t = \sigma\left[(\omega_{ih} + h_{t-1}) + (\omega_{ix} + x_t) + b_i\right] \tag{5}$$

Similarly,

$$g_{tanh} = \left(\omega_{gh} + \omega_{gx} + b_g\right) \tag{6}$$

$$g_t = tanh\left[\left(\omega_{gh} + h_{t-1}\right) + \left(\omega_{gx} + x_t\right) + b_g\right] \tag{7}$$

$$C_t^i = i_t \times g_t \tag{8}$$

$$C_t = C_t^f + C_t^i \tag{9}$$

Output gate,

$$o_{sigmoid} = (\omega_{oh} + \omega_{ox} + b_o) \tag{10}$$

$$o_t = \sigma\left[(\omega_{oh} + h_{t-1}) + (\omega_{ox} + x_t) + b_o\right] \tag{11}$$

Passing (9) through the tanh function and combining it with (11), generates the output of the hidden layer in (12):

$$h_t = tanh\,(C_t) + o_t \tag{12}$$

$$tanh\ (x) = \frac{e^x - e^{-x}}{e^x + e^{-x}} \text{ and } sigmoid\ (x) = \frac{1}{1 + e^{-x}}$$

where f_t, i_t, g_t, and o_t are forget gate, input gate, input node and output gate respectively. While ω_f, ω_i, ω_g, and $\omega_o$are the weight parameters. The bias for the gates is b_f, b_i, b_g, and b_o. σ is the sigmoid activation, which maintains the gate's output

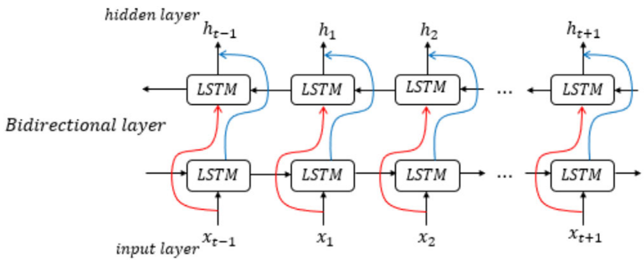

FIGURE 2 Structure of bidirectional LSTM (bi-LSTM).

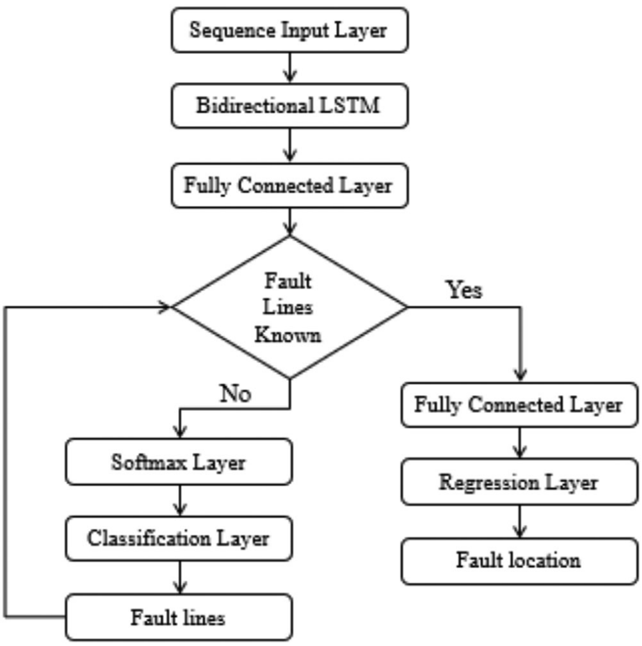

FIGURE 3 Flow diagram of bi-LSTM model.

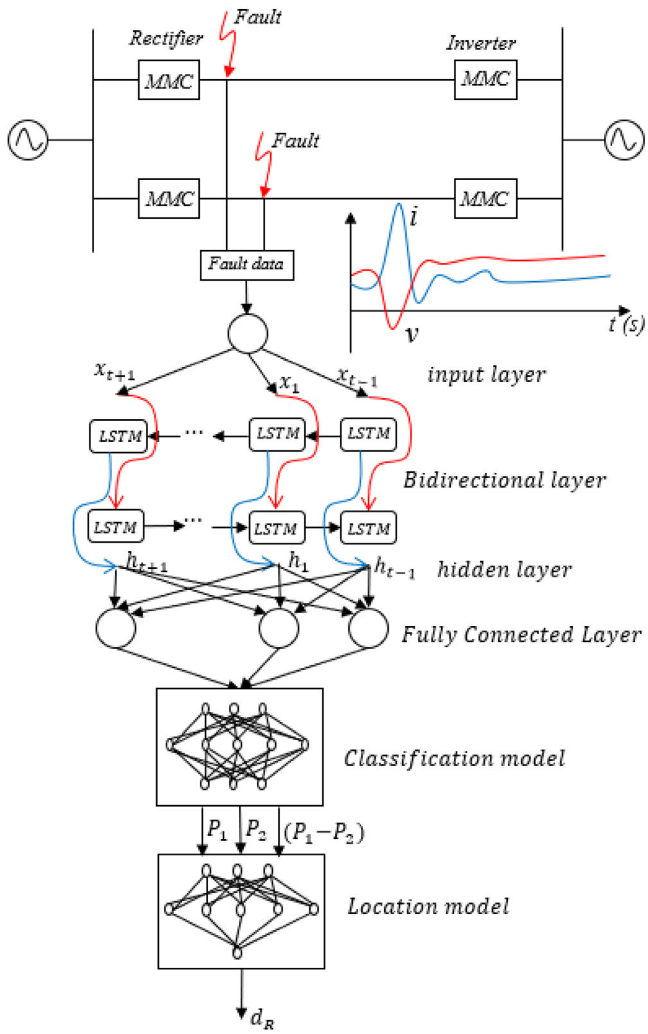

FIGURE 4 Fault location scheme.

between 0 and 1, while the tanh activation controls the outputs between −1 and 1. The current memory cell state, C_t, can be obtained from the current cell states of the input gate, C_t^i, and the forget gate, C_t^f. The latter is generated from the previous cell states of C_{t-1} and f_t. Where f_t is the combination of x_t and h_{t-1}. Setting f_t to zero ignores the old data, while setting i_t to zero ignores newly computed data. A similar computation was performed to obtain the next hidden layer of the LSTM, thus eliminating gradient disappearance.

One of the limitations of using a single LSTM is that it uses only historical data for prediction. Using a bi-LSTM, this drawback can be eliminated since the algorithm uses both the previous state (h_{t-1}) and the future state (h_{t+1}) by stacking two LSTMs in forward and backward patterns as shown in Figure 2. With this approach, the proposed algorithm can efficiently extract all the hidden layer features, thus increasing the accuracy of the location process.

The proposed bi-LSTM can classify and locate faults in MMC-HVDC transmission lines using the flow diagram shown in Figure 3. When a fault is detected in the system, the algorithm collects all fault samples from the sequence input layer. The output from the bi-LSTM layer was passed onto the fully connected layer, from which the fault types were classified, and the faulty lines were identified via the SoftMax layer. Once a faulty line is detected, the output is sent back to the fully connected layer, from which a regression layer is used to locate the fault distance.

3 | ANALYSIS OF THE FAULT LOCATION APPROACH

The proposed fault location scheme for the MMC-HVDC transmission system is shown in Figure 4. At the top of Figure 4 is a bipolar MMC system with a rectifying and inverting end. Faults such as pole1 to ground (P_1), pole2 to ground (P_2), and pole1 to pole 2 ($P_1 - P_2$) can affect the system. When a fault is detected on the transmission line, the fault current and voltage data are collected only from the rectifying end of the system into the input layer. The fault samples are passed from the input layer to the hidden layer, which comprises multiple bidirectional LSTM units, where unwanted fault samples are removed by the forget gate while the input gate updates the cell state of

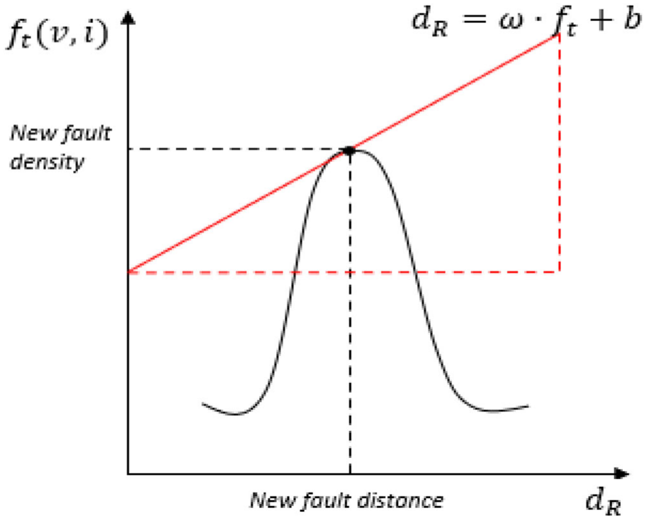

FIGURE 5 Fault location approach using a regression function.

the bi-LSTM with the maximum current and minimum voltage fault values. As a result, useful features from the fault data are extracted by the output gate. Thus, bi-LSTM improves the accuracy of the fault location scheme by providing the back-propagation needed to minimise the mean square error (MSE) in (13) and extracting the features containing the information of the faulty lines using the sigmoid and tanh activation functions.

$$MSE = \sum_{i}^{m} (D_i - d_R)^2 \tag{13}$$

where D_i is the actual location of the fault, d_R is the predicted location and m is the number of samples.

Also, from Figure 4, the output from the bi-LSTM is sent to the fully connected layer. This layer is also known as the dense layer of neurons. A fully connected layer consists of weights (ω) and bias (b) to perform dense multiplication between the input features and the trainable weights. In Figure 4, the fully connected layer can reduce the structural size of the fault samples to eliminate the computational burden and improve the speed of locating the faulty lines and the fault distance. From the fully connected layer comes the classification model. This model can classify the fault samples into different fault types (P_1, P_2, $P_1 - P_2$). The algorithm in the classification model that is responsible for detecting faulty lines is SoftMax. SoftMax can perform multiple classifications and represent the results using the probability distribution function in (14). Thus, the output is between 0 and 1, with the faulty region having the highest probability. If a fault occurs on the first transmission line, SoftMax can predict that P_1 will have a probability close to 1, while P_2 and $P_1 - P_2$ will have probabilities close to 0. Thus, all P_1 fault samples are sent to the location model to quickly obtain the fault distance.

$$SoftMax\ (P_i) = \frac{e^{x_i}}{\sum_{j=1}^{K} e^{x_j}} \tag{14}$$

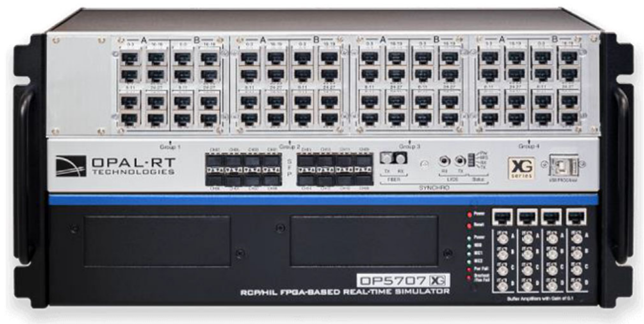

FIGURE 6 OPAL-RT Digital real-time simulator.

where e^{x_i} is the input vector standard exponential function and e^{x_j} is the output vector standard exponential function. K is the number of fault classes, and in this case, K is 3.

The fault location model uses a regression function to predict the fault distance (d_R) on the selected transmission line. d_R is measured from the point of fault impact to the rectifier substation.

Considering the fault current and voltage waveforms in Figure 4, the fault samples x_t in the input layer consisting of the current and voltage can be used to update ω and b in the regression function as shown in (15) and (16). In addition, the regression function in (17) can correlate x_t with the fault distance such that when a new fault affects the system, d_R can be obtained using (18), as shown in Figure 5.

$$\omega = \frac{N \sum t.x_t - \sum t. \sum x_t}{N \sum t^2 - \left(\sum t\right)^2} \tag{15}$$

$$b = \frac{\sum x_t}{N} - \omega. \frac{\sum t}{N} \tag{16}$$

$$f_t = \frac{1}{\sqrt{2\pi}\sigma\,(x_t - \lambda)}\, e^{\left\{-\frac{[\ln(x_t - \lambda) - \mu]^2}{2\sigma^2}\right\}} \tag{17}$$

$$d_R = \omega. f_t + b \tag{18}$$

where t is the duration of the fault, N is the number of fault samples, μ is the location parameter, σ is the standard deviation, λ is the variance, and f_t is the fault sample probability function. The point on the probability distribution curve obtained from the classification model with the highest fault sample density is used to predict the fault distance.

4 | SIMULATION SETUP AND DATA PREPARATION

In this section, the MMC-HVDC system is shown in Section 4.1, while the simulation of the faults on the systems and the extraction of the fault currents and voltages as training and test datasets are evaluated in Section 4.2.

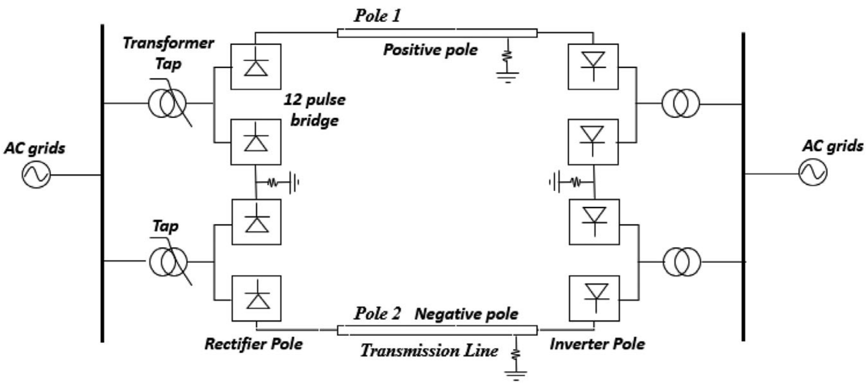

FIGURE 7 Bipolar Modular Multilevel Converter High Voltage Direct Current system.

TABLE 1 Simulation parameters for the system under test.

Design parameters	Values
AC voltage and frequency	230 kV and 60 Hz
DC voltage level	230 kV
Capacity rating	40 MW
SMs capacitor voltage	1.15 kV
Arm inductance	0.026 H
Cell capacitance	0.015 F
Number of MMC SMs	12
Insertion resistance	5 kΩ
Transmission line	DPL model—300 km, 0.79 mH/km, 0.014 uF/km, 0.02 Ω/km

4.1 | MMC-HVDC system

The validation of the fault location scheme is performed using fault samples generated from a bipolar HVDC system in Figure 7, designed in MATLAB, and simulated in real time using the OPAL-RT digital simulator shown in Figure 6. The digital simulator uses the Artemis and State Space Nodal (SSN) solver to simulate the 24-pulse bipolar HVDC on four cores of a 3.2 GHz Xeon V2 (2 cores per station).

The MMC station is a 230 kV, 40 MW, 60 Hz network based on the CIGRE Benchmark as shown in Table 1. The rectifier and inverter are 12-pulse converters connected using a bipolar link. The link (pole 1 and pole 2) is a 300-km distributed parameter line (DPL) based on frequency dependent model (FDM) [21]. The capacitance, inductance, and resistance of the line are 0.014 μF/km 0.79 mH/km, 0.02 Ω/km, respectively.

4.2 | Fault dataset generation

The first step in the fault location approach is to obtain the fault current and voltage from the network. Figure 8 shows an example of the fault current and voltage display generated from the real time simulator during the fault, from which the fault data are extracted. From the display, the fault impacted the system at 0.5 s and lasted for 0.7 s. The three different fault

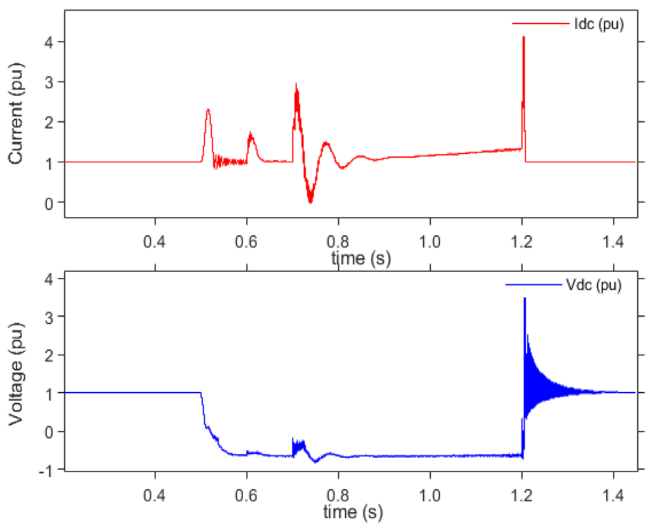

FIGURE 8 DC fault current and voltage.

types (P_1, P_2, $P_1 - P_2$) were impacted at four different inception angles (30, 45, 60, and 90) for 30 different positions of the transmission line, with 25 different resistance values selected randomly between 0.01 Ω and 250 Ω. A total of 9000 fault cases (3 fault types, 4 inception angles, 30 fault positions, and 25 fault resistances) were obtained using a sampling frequency of 12 kHz. The fault dataset was collected by a measuring relay at the rectifier pole.

The fault current and voltage samples were normalised between 0 and 1 using (19) to form the input fault samples (x_i) for the algorithm. This is done to enforce a level of uniformity without distorting the range of the values, thus improving the quality of the dataset, and speeding up the fault location process. The results of x_i obtained from the simulations are shown in Figure 9.

$$x_i = \begin{cases} \frac{i_i - \min(i)}{\max(i) - \min(i)} & \text{for fault current} \\ \frac{v_i - \min(v)}{\max(v) - \min(v)} & \text{for fault voltage} \end{cases} \tag{19}$$

Before x_i is passed to the bi-LSTM fault location scheme, it is divided into 70% training samples (6300) and 30% test

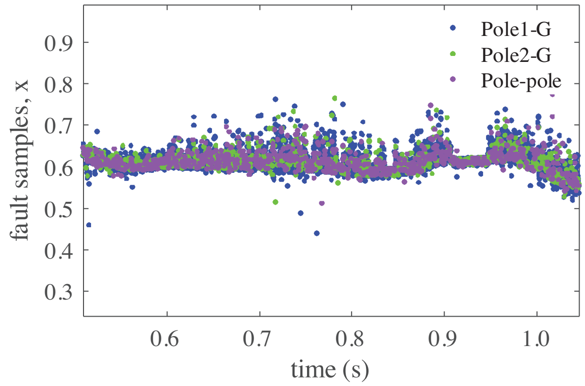

FIGURE 9 Normalised input fault samples (x).

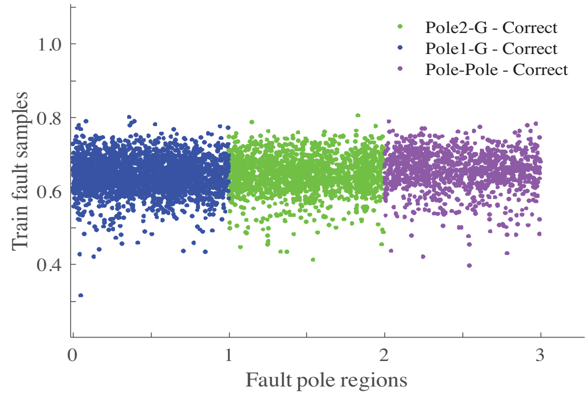

FIGURE 10 Classified trained fault samples.

samples (2700). The training fault samples are used to model the algorithm to learn and adapt to the fault features so that future predictions can be made when deployed on new fault samples, which in this case are the test samples.

For adequate training and testing, parameters such as the layers, batches, learning rate, and epochs of the bi-LSTM network should be properly selected. Increasing the number of layers, batch sizes, and epochs improves the performance of the model but adds to its complexity and computational burden, thereby increasing the locating time. Also, a learning rate that is not too low or too high should be selected because a low learning rate will converge after several iterations and thus reduce the speed of location, while a high learning rate will diverge and lead to poor accuracy [22]. Consequently, the following parameters were used for training and testing the fault datasets in a timely and accurate manner: 256 hidden layers, 3 fully connected layers, batch sizes of 90, 30 iterations (epochs), and a learning rate of 0.01.

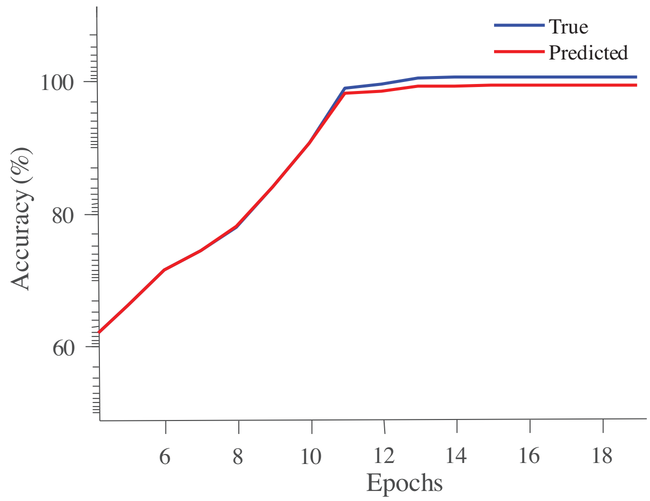

FIGURE 11 Accuracy of the trained model.

5 | SIMULATION AND RESULT

This section presents the classification model results for the training and test phases of the fault samples in Section 5.1, and the location model results are shown in Section 5.2. In Section 5.3, the effect of noise on the location scheme is analysed. In Sections 5.4 and 5.5, the bi-LSTM location scheme is deployed on a multi-terminal MMC-HVDC system to verify the scheme's robustness, while a comparative analysis with other location schemes is presented in Section 5.6.

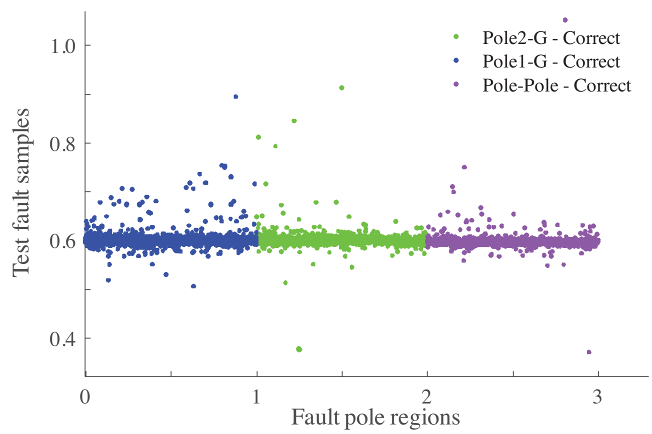

FIGURE 12 Classified test fault samples.

5.1 | Classification analysis

The classification model separates the training dataset into three different fault types (P_1, P_2, $P_1 - P_2$), as shown in Figure 10. Each fault type is identified with different regions of the transmission lines, with corresponding class intervals of 0–1, 1–2, and 2–3. The accuracy of the trained model is illustrated in Figure 11. The simulation was done for 21 iterations with a training time of 3.819 s, and it can be seen that a close comparison occurred between the actual fault regions and the classified fault types as the curves approached 100%. This verifies that the trained model has learned the fault features of the transmission and can be further deployed to predict the fault types of 2700 test samples. The identified region of the test sample is shown in Figure 12, while the performance of the prediction model is

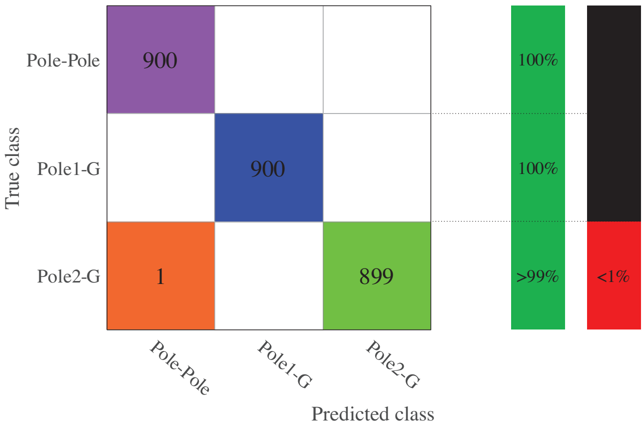

FIGURE 13 Confusion matrix of classified test model.

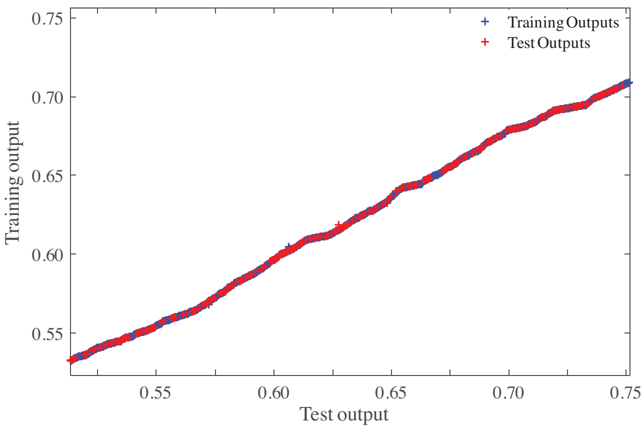

FIGURE 14 Performance of the classification model.

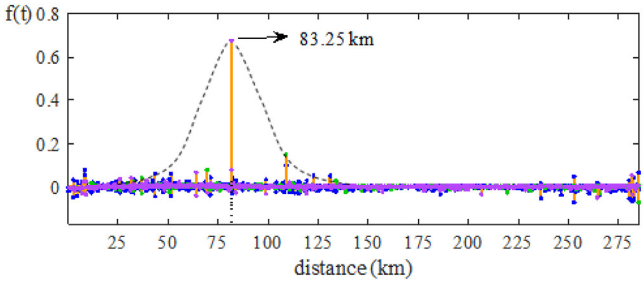

FIGURE 15 Pole-pole fault distance estimation.

shown using a confusion matrix in Figure 13. From the confusion matrix, it was observed that only one of the 900 fault samples belonging to pole2-G was incorrectly predicted.

The performance of the classification model is shown in the correlation response plot in Figure 14. The trained model was able to predict the test fault samples as both the training and test outputs converged in the three fault regions of the transmission line. Thus, the proposed classification model is accurate and efficient.

Since the fault region is known, the information from that transmission line is sent to the location model to detect the exact point of the fault impact. For example, if the classifier predicts the fault to occur on pole 1 of the bipolar network, only the pole 1 dataset is made available to the location model. This concept reduces the computational complexity of dealing with complex data from all regions of the transmission line.

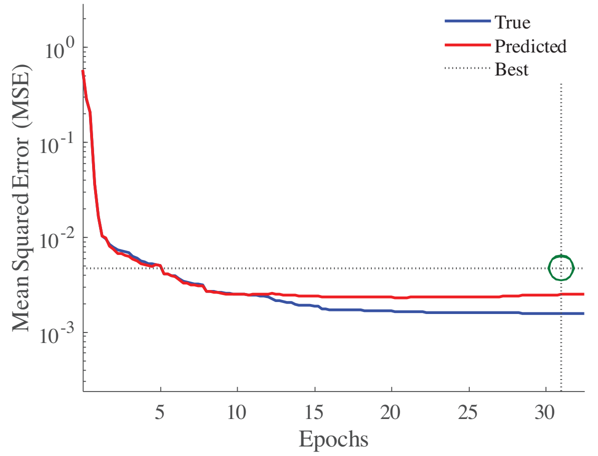

FIGURE 16 Performance of the location model in MSE.

TABLE 2 Validation of proposed location scheme.

Fault type	Actual fault location, km	Predicted fault location, km	Percentage error, %
P_1	40	39.75	0.625
	55	55.38	0.686
	108	108.22	0.203
	130	129.25	0.577
	242	242.54	0.223
P_2	50	50.16	0.319
	94	94.69	0.729
	112	111.82	0.161
	256	255.19	0.316
	287	287.86	0.299
$P_1 - P_2$	24	24.11	0.456
	73	72.39	0.836
	100	99.46	0.540
	140	139.54	0.329
	215	215.62	0.286

TABLE 3 Validation of noise data.

SNR (dB)	Actual fault location, km	Predicted fault location, km	Percentage error, %
40	40	39.644	0.890
30	80	80.73	0.904
20	160	161.49	0.923
10	240	237.72	0.950

TABLE 4 Location results for 4-terminal MMC-HVDC.

Fault lines	Actual fault location, km	Predicted fault location, km	Percentage error, %
DPL150 km	22	21.92	0.355
	70	70.33	0.469
	130	129.67	0.254
DPL200 km	50	50.47	0.931
	110	110.26	0.236
	167	165.9	0.659
	189	189.82	0.432
DPL300 km	26	26.19	0.725
	100	99.36	0.640
	265	265.68	0.256
	288	289.70	0.587
DPL400 km	80	79.35	0.813
	150	149.54	0.306
	215	216.03	0.477
	376	374.02	0.527

5.2 | Location analysis

For this study, all the test samples are sent to the location model, and considering that they were generated from faults impacted at 30 different positions, the scheme is used to predict the location of each fault impact. Figure 15 shows the distance prediction for one of the fault impacts. From the results, the distance of a pole-pole fault is indicated by a purple sample point located at the top of the probability density curve (ft). Within 1.053 ms, the model predicts the fault location at 83.25 km, since that is the distance with the highest magnitude of ft. On validation, the actual fault location was 83 km. Thus, a percentage error of 0.3% was recorded, which shows that the predicted and actual fault distances are in close agreement. Further to the above statement, Figure 16 shows the MSE of the location model. It can be seen that the curve for the predicted distance is close to the true value, with a low MSE of 0.006.

Table 2 presents the percentage error for the fault location of some of the other 29 positions. From the table, it can be seen that the percentage error for the test samples is less than 1%. This shows that the proposed location scheme has high precision for fault distance estimation.

5.3 | Performance on noisy fault data

In real-life scenarios, fault signals are sometimes contaminated with noise from measuring devices and the environment. Such distortion of the fault data can affect the accuracy of the location scheme. To verify the performance of the proposed location scheme in a noisy environment, Gaussian noise with a signal-to-noise ratio (SNR) of 40 dB to 10 dB was added to the training and test fault samples. Some of the results of the

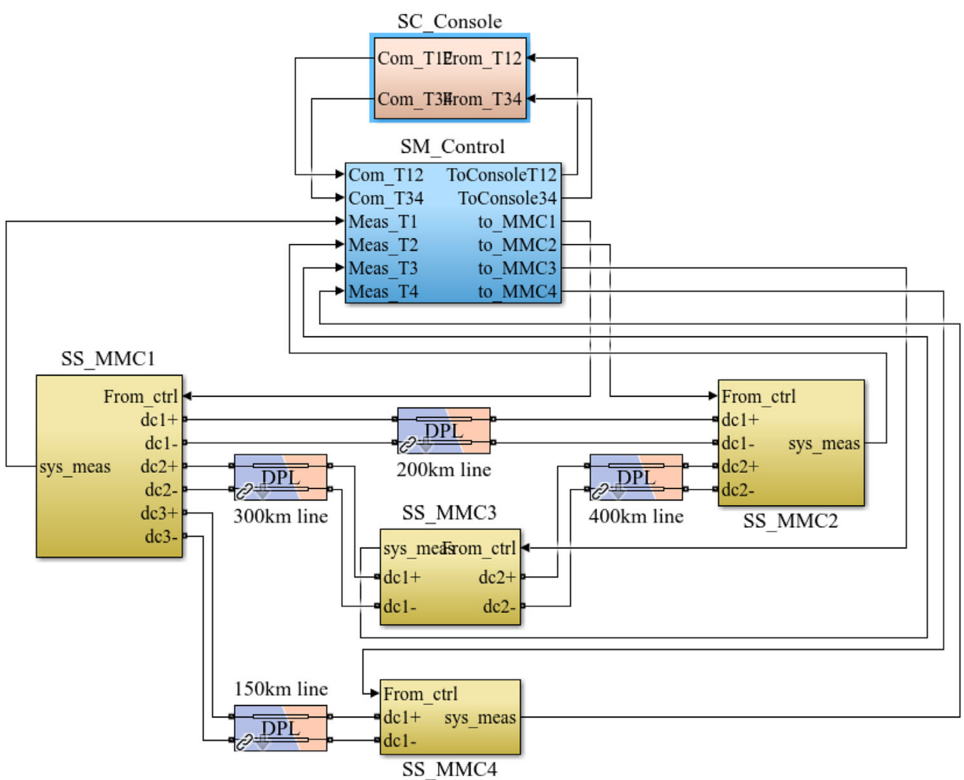

FIGURE 17 4-terminal MMC HVDC system.

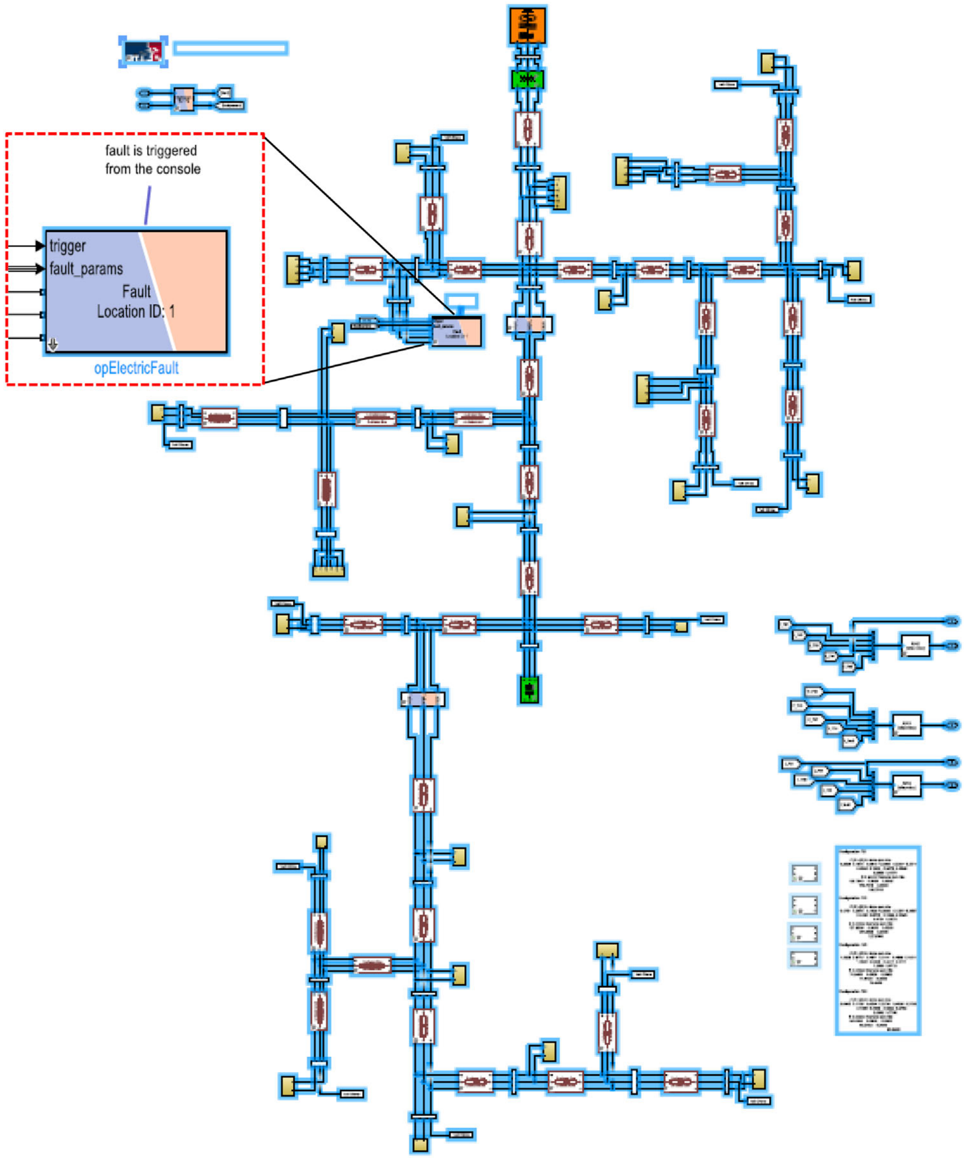

FIGURE 18 Subsystem of a 37-terminal MMC HVDC system.

distance estimation are presented in Table 3. From the table, it can be seen that the percentage error was less than 1% for the different noise levels. This verifies that the location scheme is robust to noise.

5.4 | Performance on a 4-terminal MMC-HVDC system

The proposed location scheme is deployed on a 4-terminal MMC-HVDC system based on the CIGRE benchmark. The system comprises four MMC substations with a 250 kV, 1.5 GW capacity. The MMCs are regulated by the master control (SM_Control) and connected by 4 DPL (150 km, 200 km, 300 km, and 400 km), as shown in Figure 17.

The scheme's performance is verified by simulating pole to ground faults on the four different lines. As discussed in Section 4.2, the fault data are generated by varying the resistance, distance, and inception angles. The distance prediction results obtained using the same principle as that in Section 4 are shown in Table 4. The location scheme still maintains a percentage error within 1%. Thus, the performance of the scheme is not affected by the system's complexity.

5.5 | Validation on a 37-terminal MMC HVDC system

The proposed fault location scheme is validated on an IEEE 37-terminal MMC HVDC system, simulated using the Opal-RT real-time digital simulator under unbalanced load conditions. The HVDC substation is rated at 230 kV with a capacity of 2.5 GW nominal power. Each substation is linked by different lengths of DPL transmission networks. The system uses the

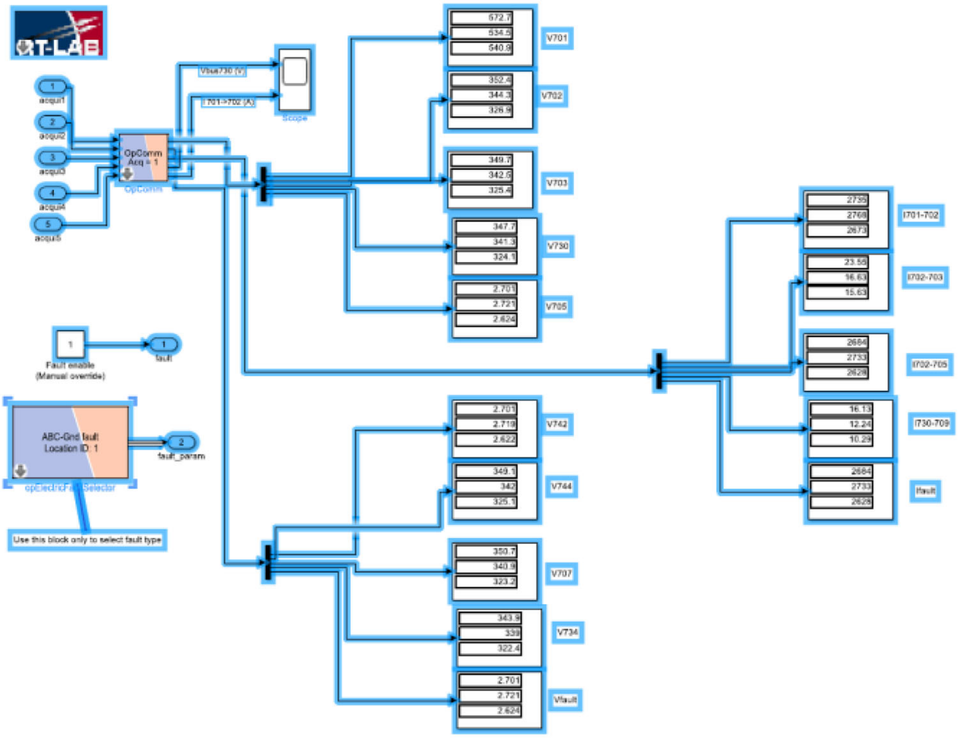

FIGURE 19 The console showing fault results.

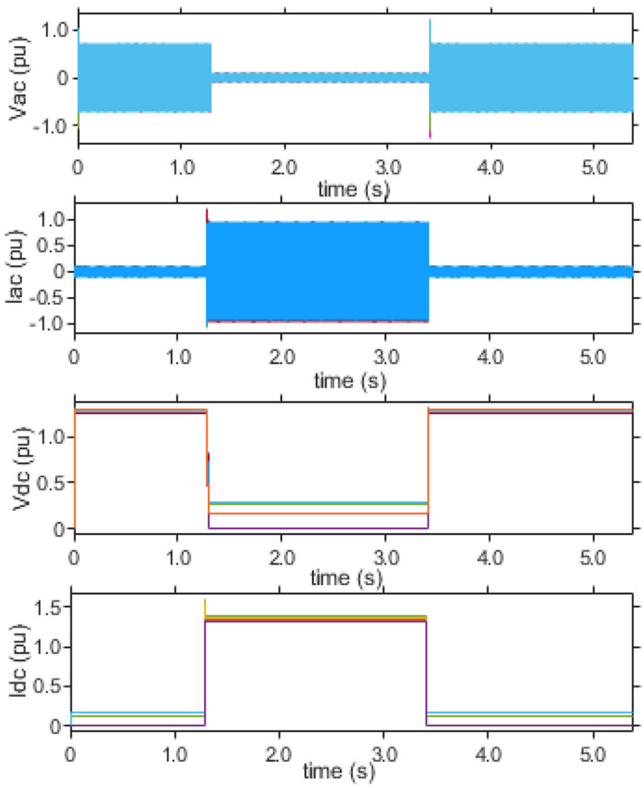

FIGURE 20 Current and voltage display of 37-terminal MMC HVDC system.

SSN solver to simulate the model and to section the model to fit into two cores containing the subsystem shown in Figure 18 and the console, which displays the fault dataset in Figure 19.

To further validate the proposed algorithm, DC faults were impacted on less than 1% and more than 99% of the transmission lines. The fault dataset was generated from a combination of different fault scenarios such as different fault locations, different fault resistances (0 Ω, 4 Ω, 8 Ω, 20 Ω, 40 Ω and 60 Ω) and different fault types (P_1, P_2, $P_1 - P_2$).

The display in Figure 20 shows a sample of the fault current and voltage obtained from ten different locations along the transmission line. The current and voltage fault data obtained from the simulation are used to train the proposed algorithm, as described in Section 4.2. The algorithm is further deployed to locate the fault points of the new fault samples.

The performance of the algorithm is further validated in Table 5 for faults that occur close to the nodes of the bus bar. From this table, it can be seen that the accuracy of the fault location algorithm drops slightly compared with its accuracy in Table 4. This is solely due to the closeness of the fault impact to the transmission line terminals, which might add some errors to the data as a result of reflections. However, the overall performance of the algorithm is still very high, with a 1% deviation in accuracy. Thus, it can be concluded that the algorithm is robust to faults occurring close to the nodes of the transmission lines. Furthermore, it can be seen that the complexity of the network has no effect on the performance of the algorithm, as the percentage error falls within the proposed 1% tolerance.

TABLE 5 Location results for 37-terminal MMC HVDC system.

	<1% of transmission line			>99% of transmission line		
Fault lines	Actual fault location, km	Predicted fault location, km	Percentage error, %	Actual fault location, km	Predicted fault location, km	Percentage error, %
DPL 701–702	0.198	0.20	1.120	19.820	20.042	1.119
DPL 702–703	0.590	0.586	0.752	59.460	59.009	0.758
DPL 703–727	0.178	0.176	1.034	17.840	17.656	1.031
DPL 703–730	0.346	0.349	0.971	34.690	35.028	0.974
DPL 704–720	0.396	0.392	0.950	39.640	39.260	0.958
DPL 706–725	0.693	0.698	0.726	69.370	68.872	0.718
DPL 707–720	0.545	0.549	0.808	54.510	54.952	0.810
DPL 709–731	0.297	0.294	0.996	29.730	29.434	0.995
DPL 714–718	0.099	0.100	1.420	9.910	9.769	1.421
DPL 733–734	0.495	0.490	0.911	49.550	50.003	0.914

TABLE 6 Comparative analyses among AI-location schemes.

Fault location methods	Communication channel requirement	Computational burden	Robustness to noise	Sampling rate	Performance (MSE)
Decision tree	No	Medium	High	Medium	0.048
K-nearest neighbour	No	Medium	High	High	0.670
ANN + fast Fourier transform	No	High	Low	High	0.889
ANN + discrete wavelet transform	No	High	High	High	0.906
SVM-based particle swarm optimisation	No	Medium	NA	High	0.590
CNN	No	High	Medium	High	0.012
Proposed bi-LSTM	No	low	High	Medium	0.006

TABLE 7 Comparative analyses among non AI-location schemes.

Fault location methods	Communication channel requirement	Computational burden	Robustness to Noise	Sampling rate	Performance (MSE)
TW	Yes	Medium	Low	High	1.990
Impedance-based	Yes	Medium	Low	High	1.206
Current differential	Yes	Medium	Low	Medium	1.405
Pearson correlation coefficient	Yes	Medium	Low	High	0.951
EMTR	Yes	High	Medium	High	1.153
Prony algorithm	Yes	High	Low	High	2.016
Voltage rate change	Yes	low	NA	Medium	2.301

5.6 | Comparisons with other location schemes

This section presents a brief comparison in Tables 6 and 7 between the existing fault location methods and the proposed scheme under the same fault scenarios. One of the parameters for comparison is the requirement for a communication channel. Location methods that require a communication channel often encounter time delays since they need time synchronisation between installed relays on each end of the network. An AI location scheme does not need to overcome these challenges. In addition, the proposed location scheme had the lowest MSE (0.006).

6 | CONCLUSION

This paper proposes a fault location scheme based on the bi-LSTM algorithm that classifies and locates faults on the transmission lines of MMC-HVDC systems with a lower sampling rate and higher performance than conventional methods. The scheme eliminates the challenges of complex data extraction and preprocessing of raw data, which could lead to a high computational burden that could affect the algorithm's performance in real engineering applications. The scheme is flexible with fault current and voltage from a single source, thus eliminating the need for a communication channel. The simulation results showed that the scheme could classify fault regions with very high accuracy, and the location model could predict fault distance with a low MSE of 0.006. In addition, the location scheme is not affected by system complexity, noise, different fault types, or resistance since the percentage error obtained from each case is within 1%.

AUTHOR CONTRIBUTIONS

The remaining authors assisted the corresponding author in organizing and proofreading the manuscript

ACKNOWLEDGEMENTS

Open access publishing facilitated by Auckland University of Technology, as part of the Wiley - Auckland University of Technology agreement via the Council of Australian University Librarians.

FUNDING INFORMATION

The authors received no specific funding information for this work.

CONFLICT OF INTEREST STATEMENT

The authors declare no conflicts of interest.

DATA AVAILABILITY STATEMENT

None.

ORCID

Jude Inwumoh https://orcid.org/0000-0003-3413-4173

REFERENCES

1. Nami, A., Liang, J., Dijkhuizen, F., Demetriades, G.D.: Modular multilevel converters for HVDC applications: review on converter cells and functionalities. IEEE Trans. Power Electron. 30(1), 18–36 (2015)
2. Pfeiffer, M., Hedtke, S., Franck, C.M.: Corona current coupling in Bipolar HVDC and hybrid HVAC/HVDC overhead lines. IEEE Trans. Power Delivery 33(1), 393–402 (2018)
3. Xue, Y., Zhang, X., Yang, C.: Series capacitor compensated AC filterless flexible LCC HVDC with enhanced power transfer under unbalanced faults. IEEE Trans. Power Syst. 34(4), 3069–3080 (2019)
4. Yang, S., Shao, Z., Zheng, W., Chen, F.: Mitigation of background harmonics effect on MMC controller based on a novel coordinate transformation technique. IEEE Access 7,167113–167126 (2019)
5. Ansari, J.A., Liu, C., Khan, S.A.: MMC based MTDC grids: A detailed review on issues and challenges for operation, control and protection schemes. IEEE Access 8, 168154–168165 (2020)
6. Reid, F.. Trip of transmission lines in tasmania followed by the loss of basslink on 10 and 16 Dec 2014, and 23 Feb 2015. (2015)
7. Zhang, C., Song, G., Wang, T., Yang, L.: Single-ended traveling wave fault location method in dc transmission line based on wave front information. IEEE Trans. Power Delivery 34(5), 2028–2038 (2019)
8. Jia H. An improved traveling-wave-based fault location method with compensating the dispersion effect of traveling wave in wavelet domain. Math. Probl. Eng. 2017, 1019591. (2017)
9. Ahmadimanesh, A., Shahrtash, S.M.: Transient-based fault-location method for multiterminal lines employing S-transform. IEEE Trans. Power Delivery. 28(3), 1373–1380 (2013)
10. Lin, S., Liu, L., Sun, P., Lei, Y., Teng, Y., Li, X.: Fault location algorithm based on characteristic- harmonic measured impedance for hvdc grounding electrode lines. IEEE Trans. Instrum. Meas. 69(12), 9578–9585 (2020)
11. Farshad, M., Sadeh, J.: A novel fault-location method for HVDC transmission lines based on similarity measure of voltage signals. IEEE Trans. Power Delivery. 28(4), 2483–2490 (2013)
12. Wang, Z., Razzaghi, R., Paolone, M., Rachidi, F.: Electromagnetic time reversal similarity characteristics and its application to locating faults in power networks. IEEE Trans. Power Delivery 35(4), 1735–1748 (2020)
13. Wang, L., Huang, L., Huang, P.H., et al.: Fault location method for DC hybrid line based on VMD-backward prediction Prony. Power Grid Clean Energy 36(10), 61–67 (2020)
14. Chen, Y.Q., Fink, O., Sansavini, G.: Combined fault location and classification for power transmission lines fault diagnosis with integrated feature extraction. IEEE Trans. Ind. Electron. 65(1), 561–569 (2018)
15. Swetapadma, A., Yadav, A.: A novel decision tree regression-based fault distance estimation scheme for transmission lines. IEEE Trans. Power Delivery 32(1), 234–245 (2017)
16. Livani, H., Evrenosoglu, C.Y.: A single-ended fault location method for segmented HVDC transmission line. Electr. Power Syst. Res. 107, 190–198 (2014)
17. Psaras, V., Tzelepis, D., Burt, G.: HVDC grid fault location method using genetic algorithm on reconstructed frequency-domain voltage profiles. Int. J. Electr. Power Energy Syst. 144, 108429. (2023)
18. Guo, L., Lei, Y., Xing, S., Yan, T., Li, N.: Deep convolutional transfer learning network: A new method for intelligent fault diagnosis of machines with unlabeled data. IEEE Trans. Ind. Electron. 66(9), 7316-7325. (2018)
19. Lan, S., Chen, M.-J., Chen, D.-Y.: A novel HVDC double-terminal non-synchronous fault location method based on convolutional neural network. IEEE Trans. Power Delivery 34(3), 848–857 (2019)
20. Dittmer, S., King, E.J., Maass, P.: Singular values for ReLU layers. IEEE Trans. Neural Networks Learn. Syst. 31(9), 3594–3605 (2020)
21. Martí, J.R., Tavighi, A.: Frequency-dependent multiconductor transmission line model with collocated voltage and current propagation. IEEE Trans. Power Delivery 33(1), 71–81 (2018)
22. Wang, Y., Liu, J., Mišić, J., Mišić, V.B., Lv, S., Chang, X.: Assessing optimizer impact on DNN model sensitivity to adversarial examples. IEEE Access 7, 152766–152776 (2019)

How to cite this article: Inwumoh, J., Baguley, C., Madawala, U., Gunawardane, K.: A novel fault location strategy based on Bi-LSTM for MMC-HVDC systems. J. Eng. 2023, e12310 (2023). https://doi.org/10.1049/tje2.12310